The effect of hydrogen-bond interactions on the electronic nature of DPP-based organic semiconductors: Implications on charge transport

Raúl González-Núñez, [a], Gabriel Martinez, [b], Nelson Ricardo Avila-Rovelo, [b,c] Kyeog-Im Hong, [b,d,e], Amparo Ruiz-Carretero,[b],[d] Rocío Ponce Ortiz [a]**

[a] Department of Physical Chemistry, University of Málaga, Campus de Teatinos s/n, Málaga 29071, Spain.

[b] University of Strasbourg, Institute Charles Sadron, CNRS, UPR22, 23 Rue du Loess, 67034, Strasbourg Cedex 2, France.

[c] Current affiliation: Institute for Chemistry and Processes for Energy, Environment and Health, ICPEES, UMR 7515, 25 Rue Becquerel, 67087, Strasbourg Cedex 2, France

[d] Instituto de Ciencia de Materiales de Madrid, Consejo Superior de Investigaciones Científicas CSIC, Sor Juana Inés de la Cruz 3, 28049, Madrid, Spain

[e] Current affiliation: Instituto Madrileño de Estudios Avanzados, IMDEA Nanoscience, Calle Faraday 9, 28049, Madrid, Spain

Table of Contents

1. Synthesis and characterization

Molecules **HDPPBA-C**, **HDPPBA-N** and **HDPPH** were synthesized and characterized according to a previously reported protocol. [1]

2. Molecular and Supramolecular Characterization

Theoretical calculations for **HDPPBA-C**, **HDPPBA-N** and **HDPPH** derivates were carried out in the frame of density functional theory (DFT), using the B3LYP[2,3] functional and the 6-31G** basis[4,5] set as implemented in the Gaussian 16 program. Geometry optimizations were performed without any symmetry constrains. Based on the resulting ground-state geometries, harmonic vibrational frequencies and TD-DFT were calculated at the same theoretical level.

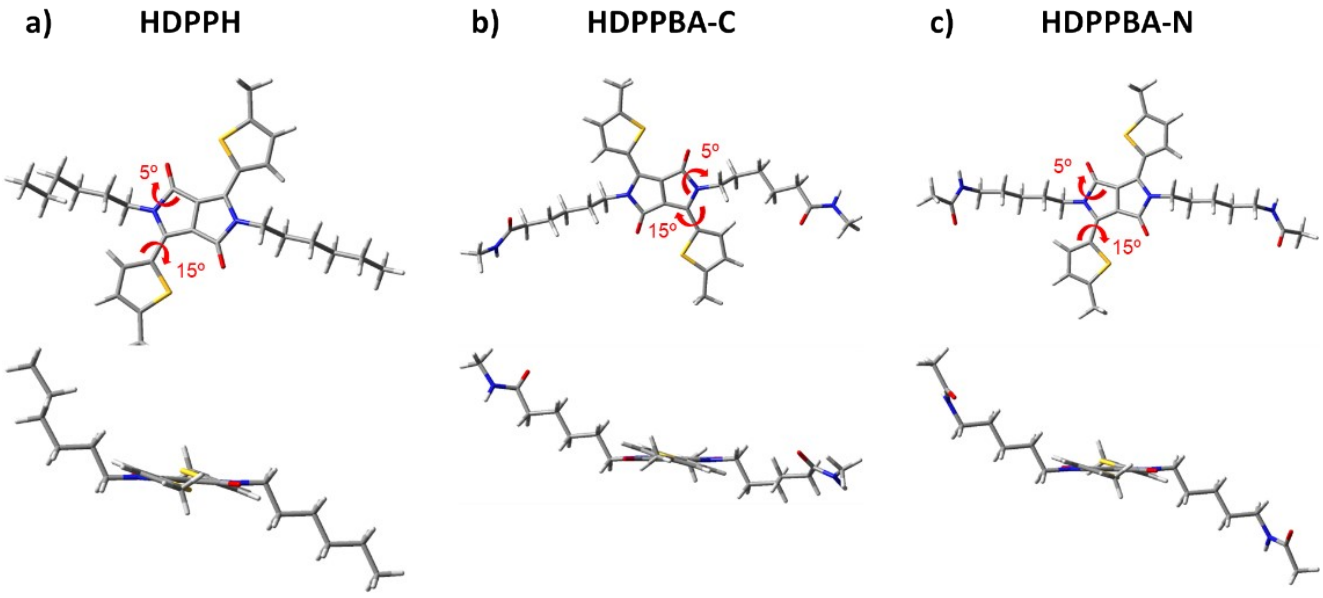

Figure S1. DFT//B3LYP/6-31G** optimized molecular structures of a) **HDPPH**, b) **HDPPBA-C** and c) **HDPPBA-N**.

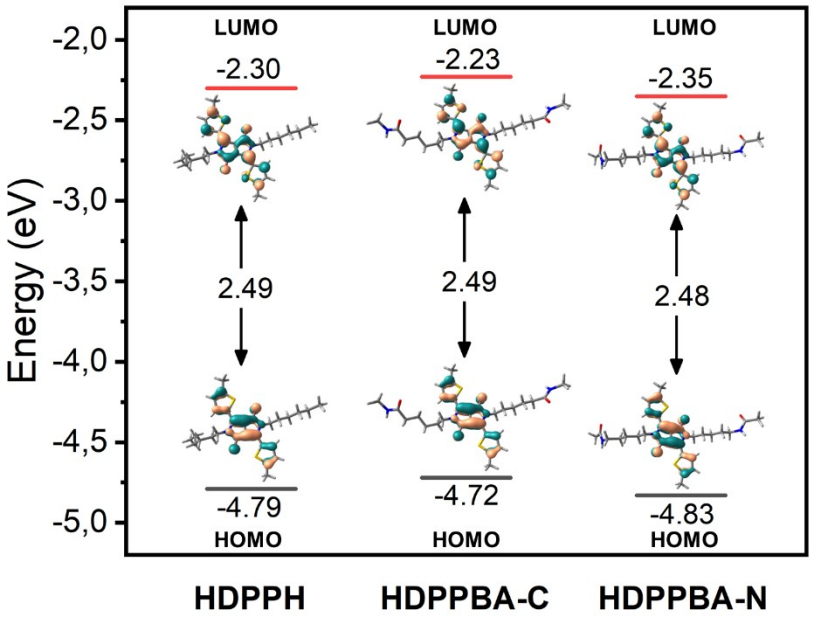

Figure S2. DFT-calculated molecular orbital energies (B3LYP/6-31G**) for the studied molecules along with topologies of the HOMO and LUMO orbitals.

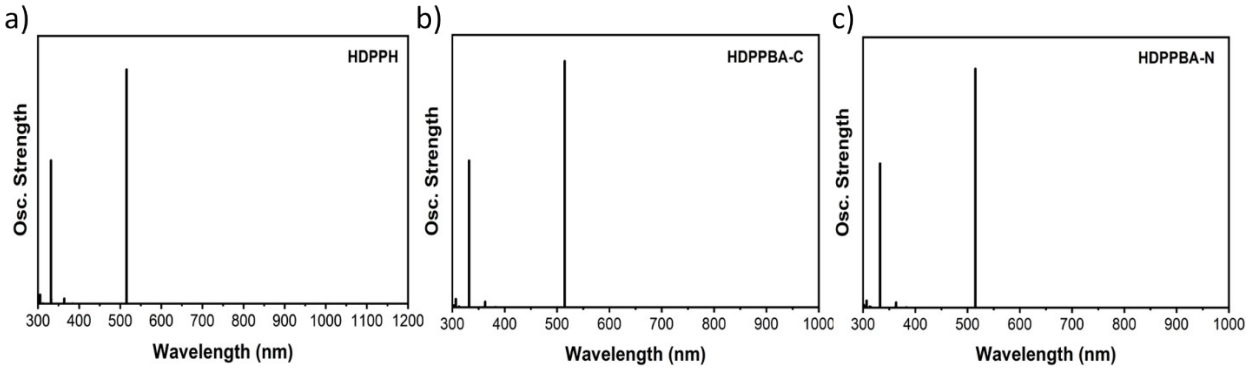

Figure S3. TD-DFT calculated vertical transition energies of HDPPH (a), HDPPBA-C (b) and HDPPBA-N (c) determined at B3LYP/6-31G** level of theory.

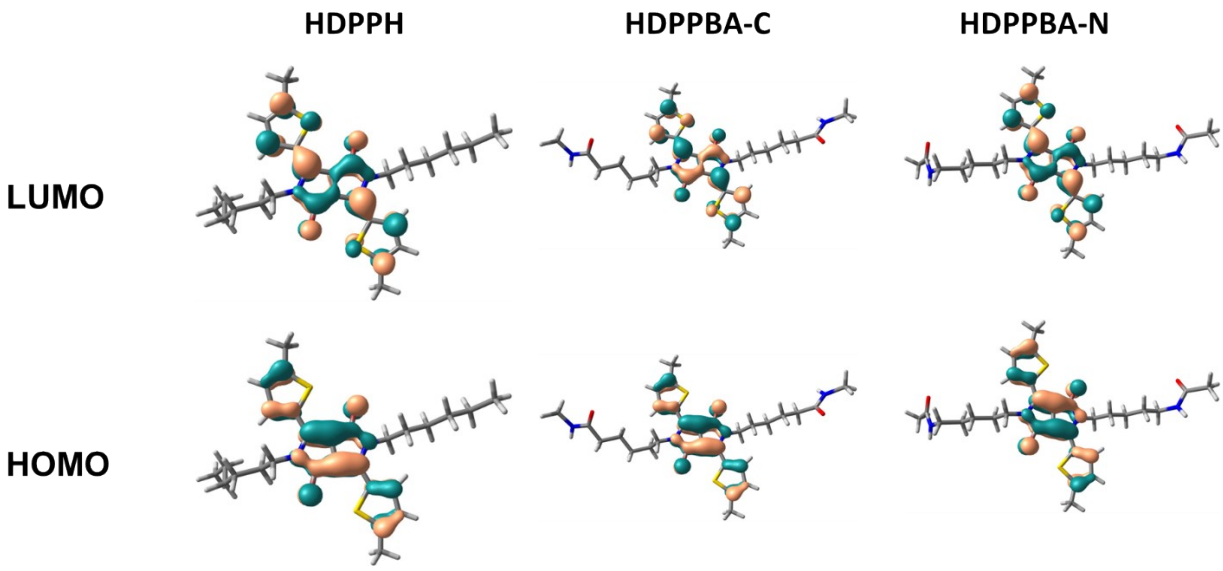

Figure S4. Molecular orbital topologies of HOMO and LUMO orbitals of HDPPH, HDPPBA-C, and HDPPBA-N (isovalue of 0.035 a.u).

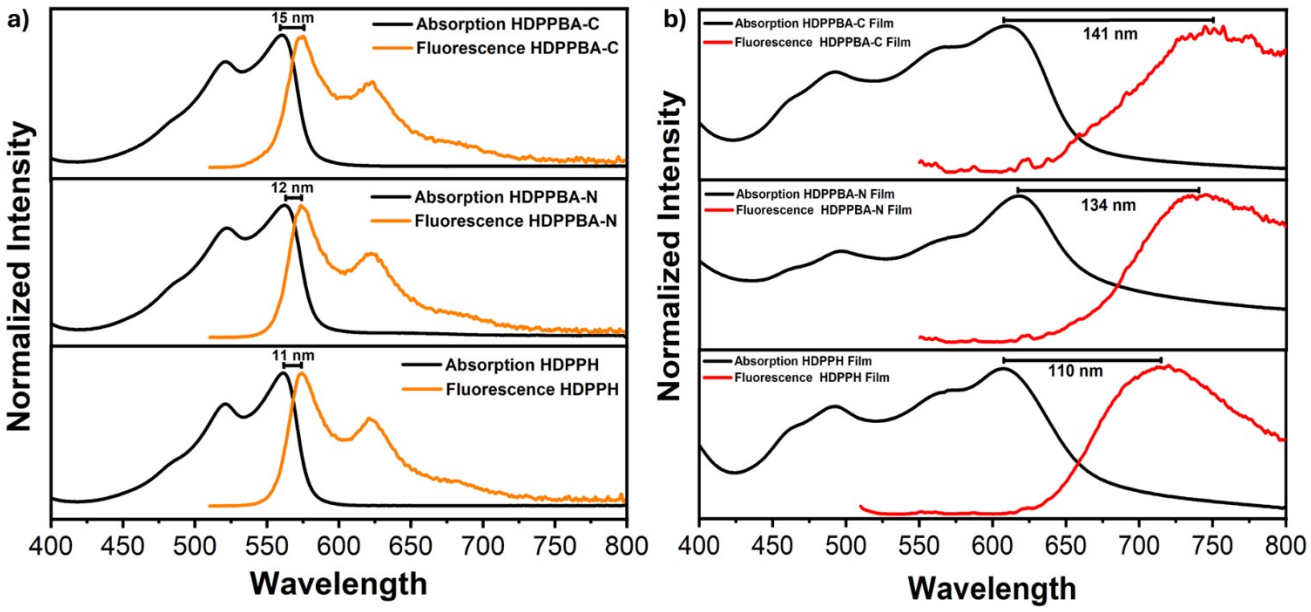

Figure S5. a) UV-Vis absorption spectra in chloroform solution (black) and emission spectra (orange) of **HDPPH**, **HDPPBA-C** and **HDPPBA-N**. b) UV-Vis absorption spectra in film (black) and emission spectra in film (red) of **HDPPH**, **HDPPBA-C** and **HDPPBA-N**.

Cyclic voltammetry measurements were carried out under an atmosphere of argon using a three-electrode arrangement in a single compartment cell. A platinum disc working electrode, a platinum wire counter electrode and a non-aqueous Ag/Ag^+ reference electrode were used in the cell using an Ossila potentiostat. Redox potentials are quoted versus the ferrocenium-ferrocene couple, which was used as an internal reference, 100 mV/s scan rate. CH_2Cl_2 (dried and degassed) was utilized as solvent with tetrabutylammonium hexafluorophosphate ($TBAPF_6$, 0.1 M) employed as supporting electrolyte**.**

CV experiments in thin film were carried out in acetonitrile containing of 0.2 M TBAPF6 as a supporting electrolyte, at a potential scan rate of 100 mVs^{-1} and using a micro-Autolab type III equipment provided from Metrohm (Figure 2). A leakless Ag/AgCl electrode was used as the reference electrode. Pt wire was used as counter electrode. A 1 mM solution of the studied semiconductors in chloroform were drop-casted onto a glassy carbon working electrode. The obtained redox potentials were calibrated with the ferrocene/ferrocenium (Fc/Fc+) redox couple.

HOMO and LUMO levels were calculated using the equations:

E_{HOMO} = - (E_{onset}(ox) + 4.8 [eV]) and E_{LUMO} = -(E_{onset}(red) + 4.8 [eV]).

The band gap is calculated using the equation

Eg = E_{HOMO} - E_{LUMO} [eV].

Table S1. Cyclic voltammetry data recorded in DCM/TBAPF6 (0.1 M) at a scan rate of 100 mV/s using Pt as working and the counter electrode, and Ag/Ag^+ as reference.

Derivative	E_{HOMO} (eV)	E_{LUMO} (eV)	E_g (eV)
HDPPH	-5.08	-3.49	1.59
HDPPBA-C	-5.08	-3.46	1.62
HDPPBA-N	-5.16	-3.50	1.63
HDPPH Film	-5.21	-3.68	1.53
HDPPBA-C Film	-5.13	-3.63	1.50
HDPPBA-N Film	-5.16	-3.59	1.57

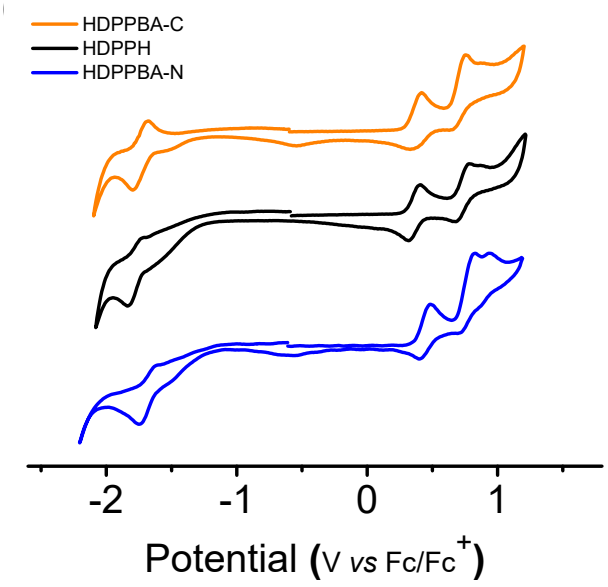

Figure S6. Cyclic voltammograms of HDPPH, HDPPBA-C and HDPPBA-N (1 mM) full sweep of at 100 mV/s scan rate (referenced against potential of Fc/Fc+) in CH_2Cl_2 with tetrabutylammonium hexafluorophosphate 0.1 M as supporting electrolyte.

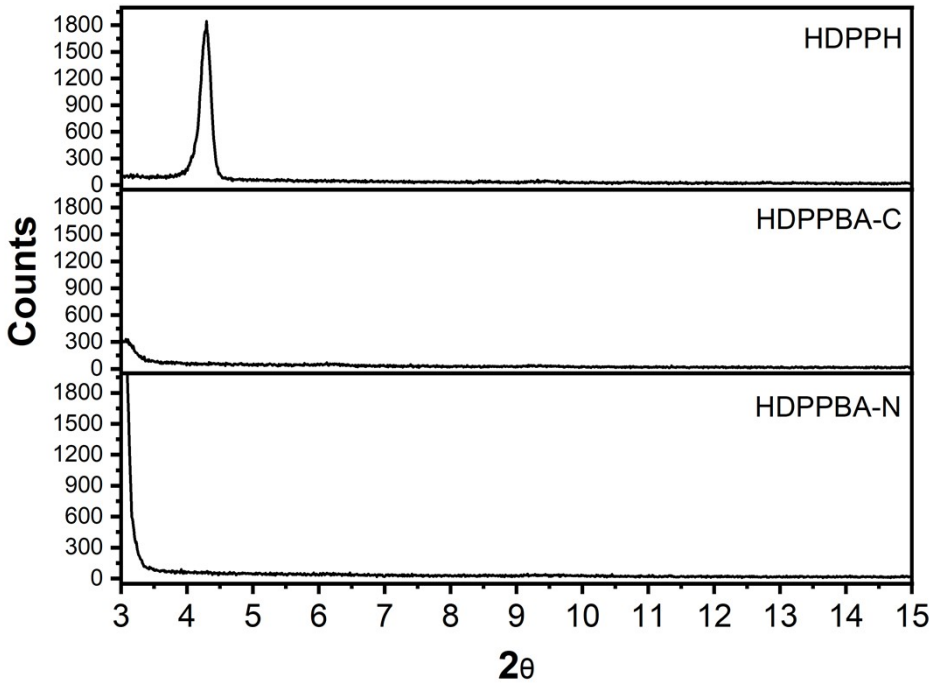

Figure S7. Θ-2Θ X-ray diffraction scans of solution deposited **HDPPBA-C**, **HDPPBA-N** and **HDPPH** thin films grown on OTS-treated Si/SiO2 substrates.

3. Thermal Study

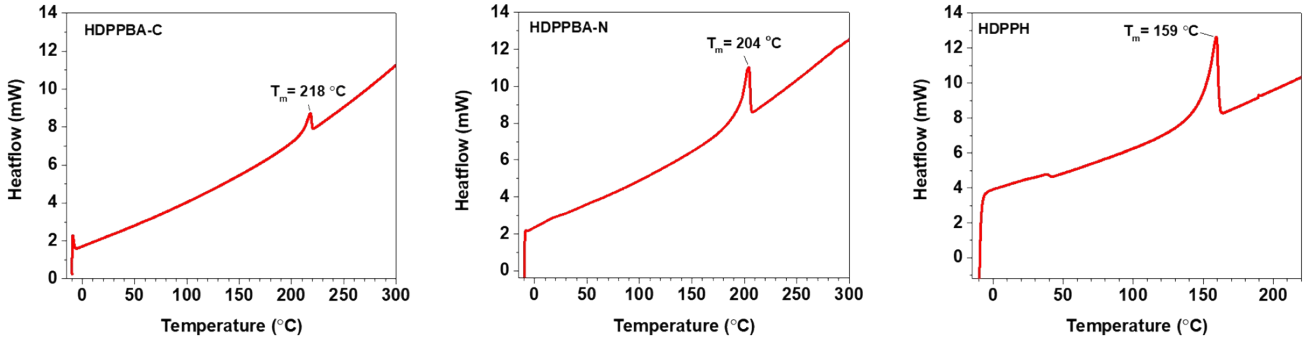

Figure S8. DSC measurements for **HDPPBA-C**, **HDPPBA-N** and **HDPPH**

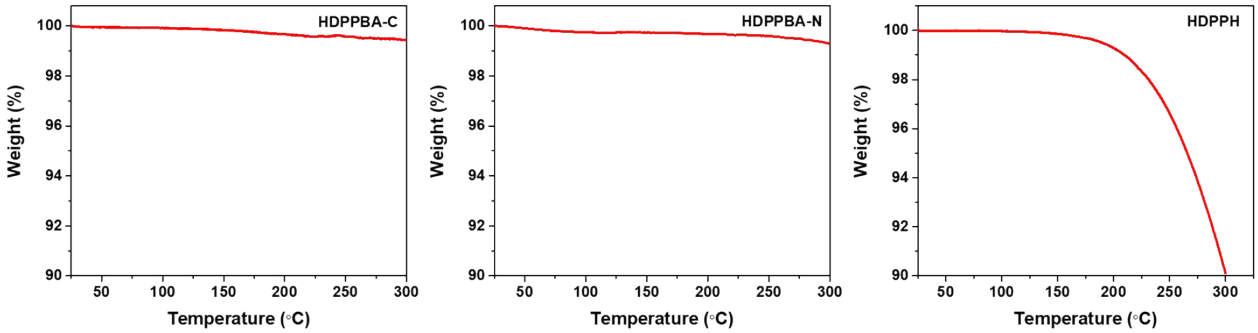

Figure S9. TGA measurements for **HDPPBA-C**, **HDPPBA-N** and **HDPPH**

4. Organic field-effect transistor fabrication and characterization

To evaluate the efficiency of these molecules as charge carriers, organic field-effect transistors have been fabricated in a top-contact/bottom-gate structure. The device parameters, such as, the charged mobilities (μ), threshold voltage (V_T) and current on/off ratio (I_{ON} /I_{OFF}) were extracted from the saturated region in the device transfer curves using conventional transistors formalisms (eq (1))

$$I_{DS} = \frac{WC\mu}{2L}(V_G - V_T)^2 \qquad (1)$$

Where I_{DS} correspond to the drain current in the saturation regime, W to the channel width, L to the channel length, C is the capacitance per unit area of the insulator layer, and V_G the gate voltage.

The deposition of the active semiconducting film for the three compounds (**HDPPBA-C**, **HDPPBA-N** and **HDPPH**) has been carried out by drop casting from different solutions with a concentration of 5 mg/ml in different solvents (chloroform, 1,2-dichlorobenzene, tetrahydrofuran (THF) and toluene, as well as different mixtures of these) at room temperature on a gate dielectric (d-doped Si wafers with 300 nm thermally grown SiO_2 dielectric layer) previously functionalized with hexamethyldisilazane (HMDS) and octadecyltrichlorosilane (OTS) self-assembled monolayers (Table S1). The capacitance of the 300 nm SiO_2 gate insulator was 10 $nFcm^{-2}$. Prior the surface functionalization, the wafers were solvent cleaned by immersing them twice for 10 min in EtOH with sonication, drying with a stream N_2, and treating with UV-ozone for 10 min. For HMDS treatment, the cleaned silicon wafers were exposed to HMDS vapor at room temperature in closed air-free container under argon for a week, and for OTS treatment, the cleaned silicon wafers were immersed in OTS solution (3 mM) during 2 hours, after, the wafers were cleaned with hexane, acetone and EtOH respectively for 10 min with sonication and drying with a stream N_2. Subsequently of the deposition of active semiconducting films, OFETs devices were completed by gold vapor deposition through a shadow mask to define devices with various channel lengths and channel widths. Prior the electrode deposition, some of the substrates were subjected to a heat treatment (120 ºC during 3 hours), in order to modify the semiconducting thin film morphology and long-range order and thus improve the OFET performance parameters.

The devices were characterized under vacuum (in a customized probe station) with a 4200-SCS/C Keithley semiconductor characterization system.

The film layers were characterized by AFM (Figure S1) and GIXRD (Figure S2) measurements. AFM images were recorded by Multimode atomic force microscope with a Nanoscope V controller (Bruker Corporation, Billerica, MA, USA) working in tapping mode.

GIXRD data using CuKα1 radiation was recorded by using a Bruker D8 DISCOVER diffractometer. The grazing incidence X-ray diffraction setup is equipped with a parabolic Göbel mirror and a conventional line focus Cu radiation tube (40 kV/40mA).

Table S2. P-channel OFET derived electrical data for **HDPPH, HDPPBA-C** and **HDPPBA-N**. The best values and average (in parenthesis) are shown. The average values were obtained from at least 5 devices for each material.

Solvent	Compound	Subst. treatment	μ_h ($cm^2 V^{-1} s^{-1}$)	V_T(V)	I_{ON}/I_{OFF}
$CHCl_3$	**HDPPH**	NA	NA	NA	NA
	HDPPBA-C	OTS (120)	$2x10^{-2}$	-12	$2x10^{+4}$
	HDPPBA-C	OTS (200)	$6x10^{-3}$	-19	$6x10^{+4}$
	HDPPBA-C	OTS (230)	NA	NA	NA
	HDPPBA-N	OTS (120)	$1x10^{-2}$	-3	$4x10^{+5}$
	HDPPBA-N	OTS (200)	$7x10^{-3}$	-15	$2x10^{+4}$
	HDPPBA-N	OTS (230)	NA	NA	NA
1,2-diClBz	**HDPPH**	NA	NA	NA	NA
	HDPPBA-C	HMDS	$1x10^{-3}$	-20	$2x10^{+3}$
	HDPPBA-N	HMDS (120)	$3x10^{-4}$	-24	$1x10^{+2}$
THF	**HDPPH**	NA	NA	NA	NA
	HDPPBA-C	OTS (120)	$1x10^{-3}$	-39	$3x10^{+2}$
	HDPPBA-N	HMDS (120)	$1x10^{-4}$	-10	38
CHCl3/Toluene (9:1)	**HDPPH**	NA	NA	NA	NA
	HDPPBA-C	HMDS (120)	$3x10^{-3}$	-13	$1x10^{+4}$
	HDPPBA-N	HMDS (120)	$3x10^{-4}$	-15	$6x10^{+2}$
$CHCl_3$/ 1,2-diClBz (8:2)	**HDPPH**	NA	NA	NA	NA
	HDPPBA-C	OTS (120)	$3x10^{-4}$	-18	$4x10^{+2}$
	HDPPBA-N	OTS	$6x10^{-5}$	-23	$5x10^{+1}$

5. Vibrational spectroscopy

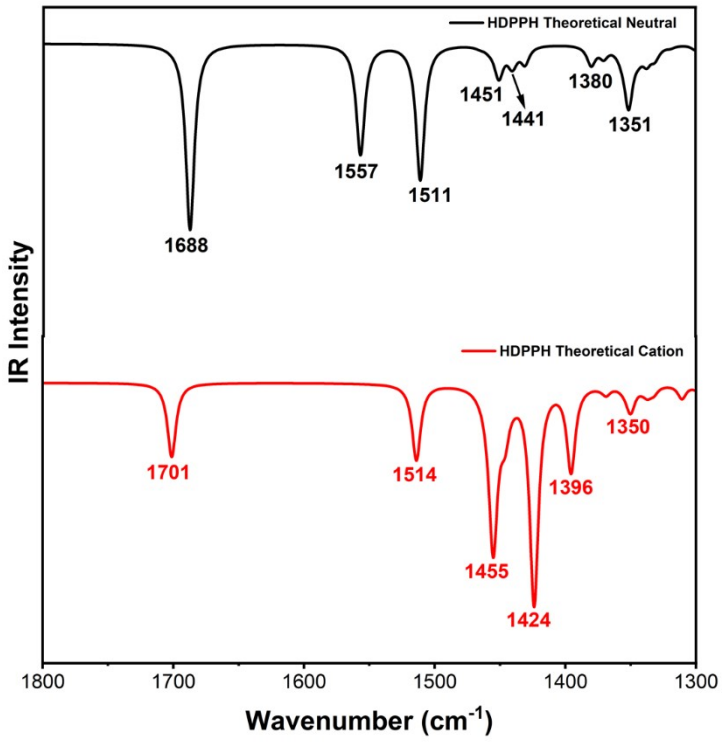

Figure S10. B3LYP/6-31G** IR theoretical spectra (*f*=0.96) for **HDPPH.** Black for neutral state and red for radical cation state.

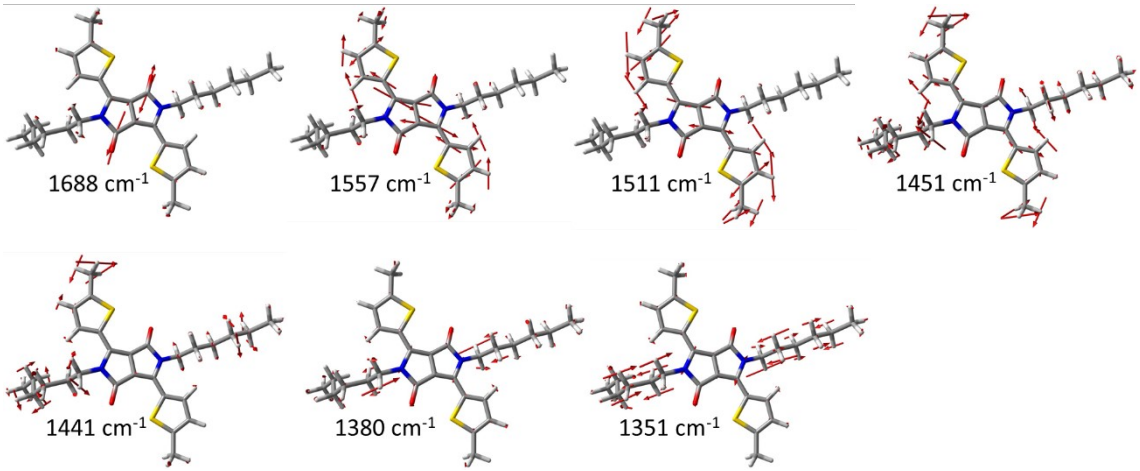

Figure S11. B3LYP/6-31G** IR predicted eigenvectors for **HDPPH** in neutral state

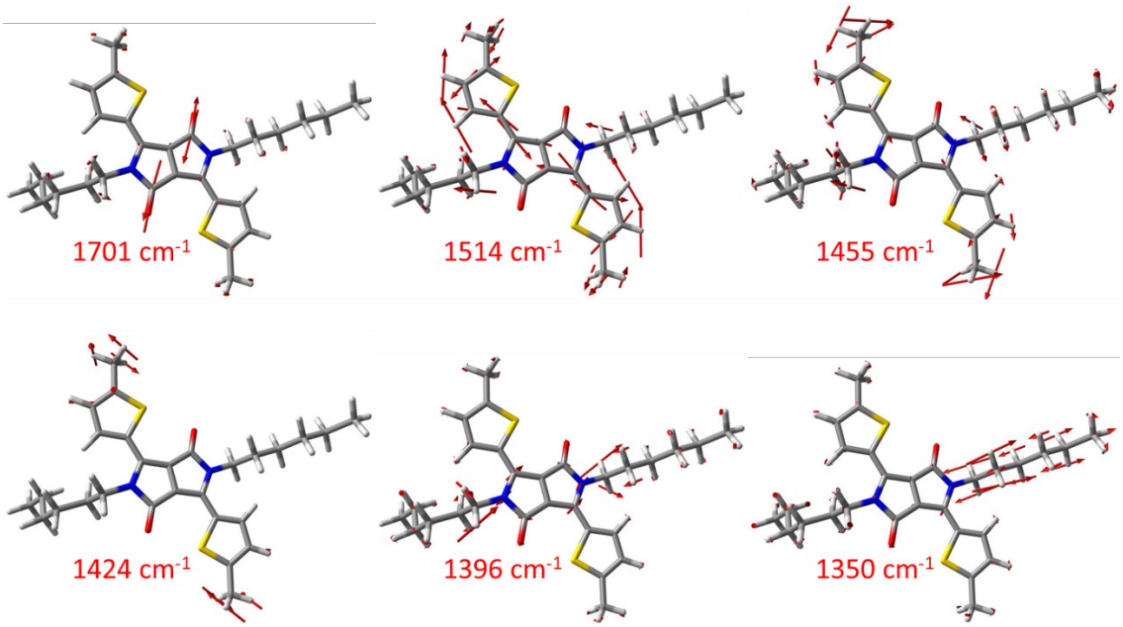

Figure S12. B3LYP/6-31G** IR predicted eigenvectors for **HDPPH** in radical cation state.

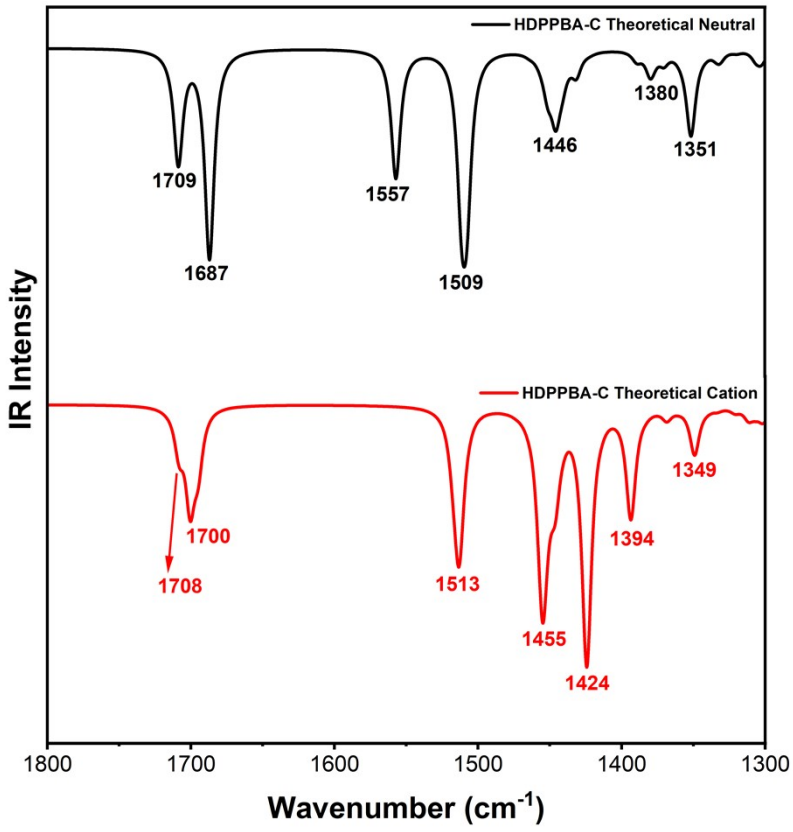

Figure S13. B3LYP/6-31G** IR theoretical spectra (*f*=0.96) for **HDPPBA-C** as neutral and radical cation species.

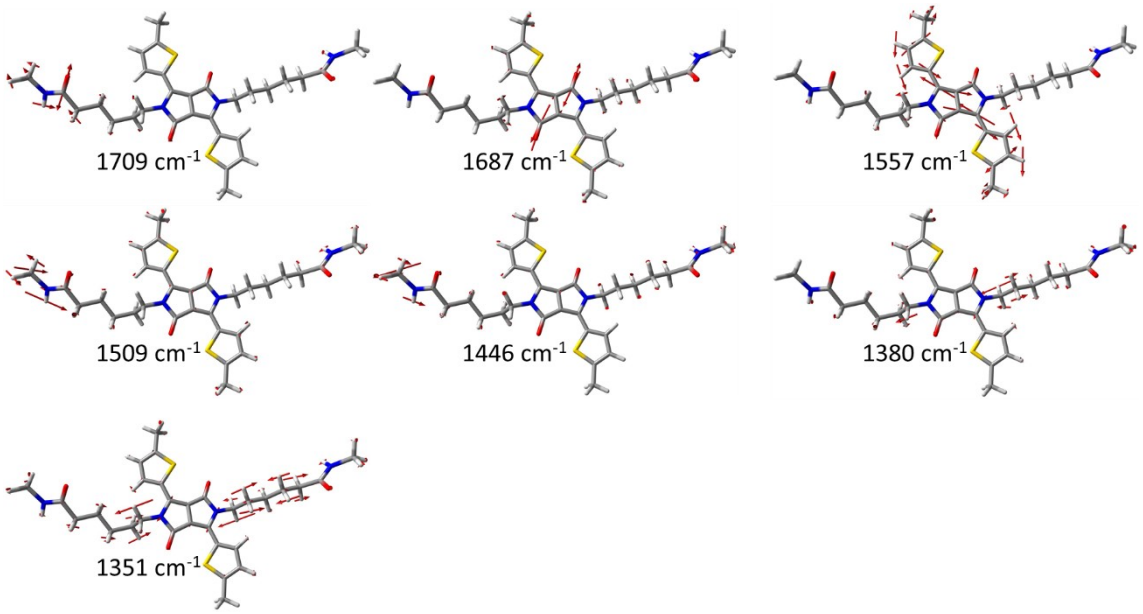

Figure S14. B3LYP/6-31G** IR predicted eigenvectors for **HDPPBA-C** in neutral state.

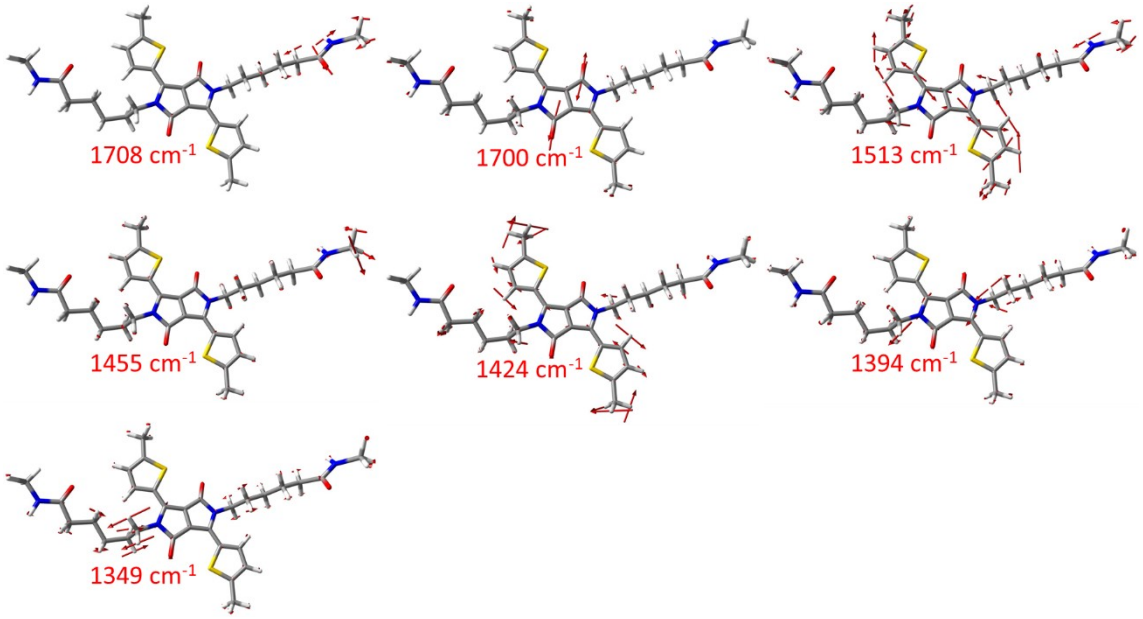

Figure S15. B3LYP/6-31G** IR predicted eigenvectors for **HDPPBA-C** in radical cation state.

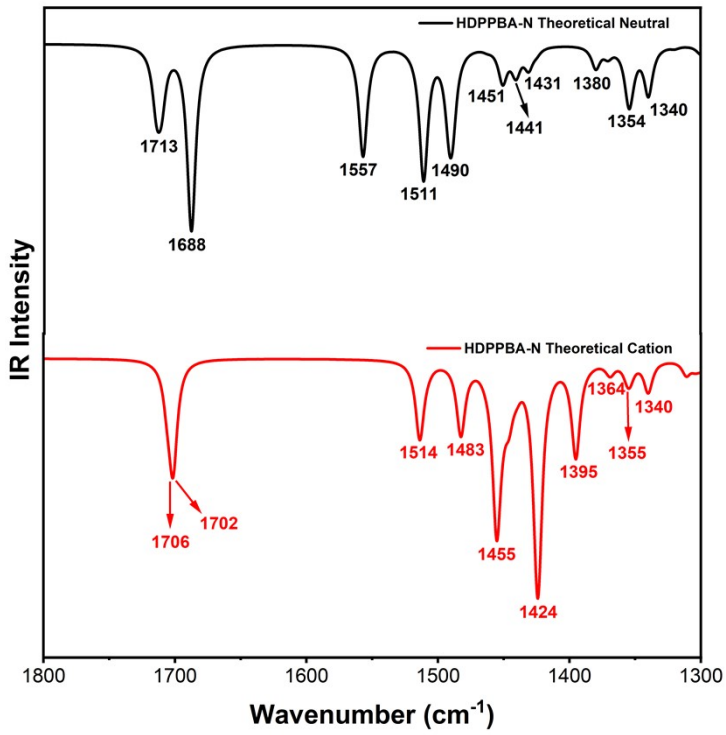

Figure S16. B3LYP/6-31G** IR theoretical spectra (*f*=0.96) for **HDPPBA-N** for neutral and radical cation species.

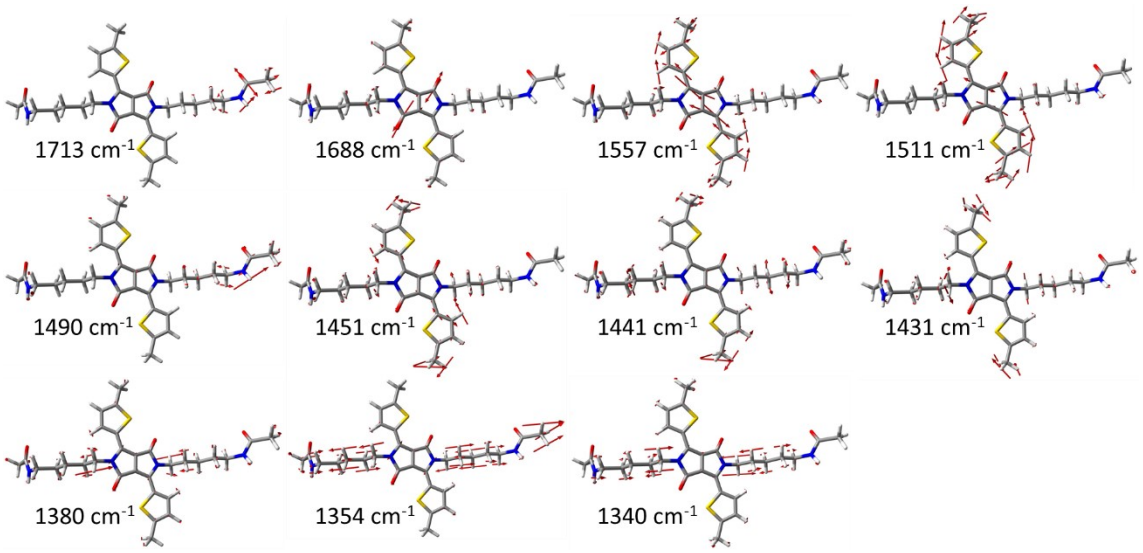

Figure S17. B3LYP/6-31G** IR predicted eigenvectors for **HDPPBA-N** in neutral state.

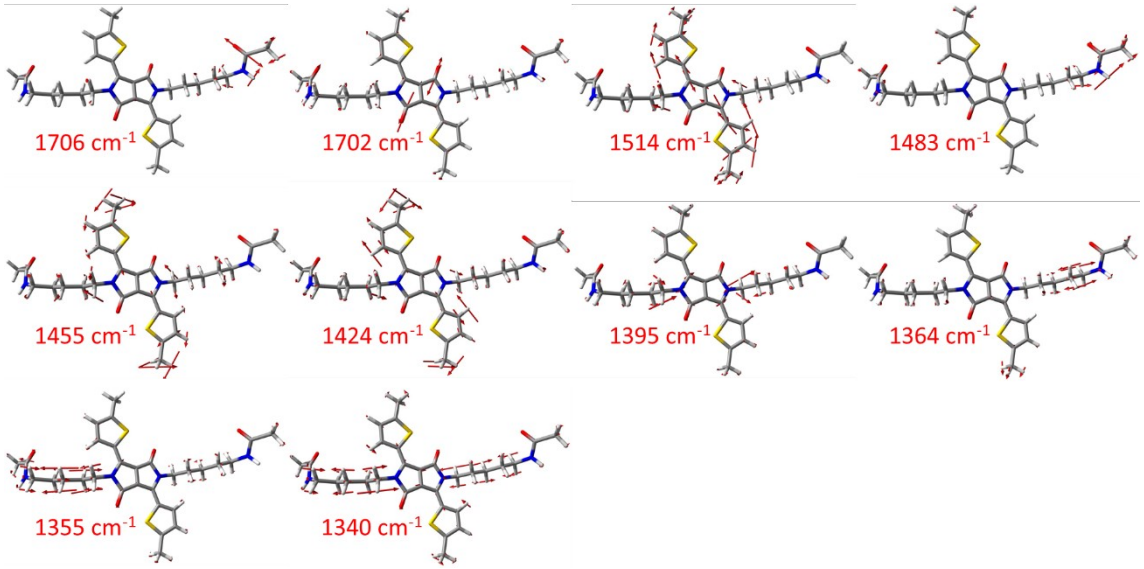

Figure S18. B3LYP/6-31G** IR predicted eigenvectors for **HDPPBA-N** in radical cation state.

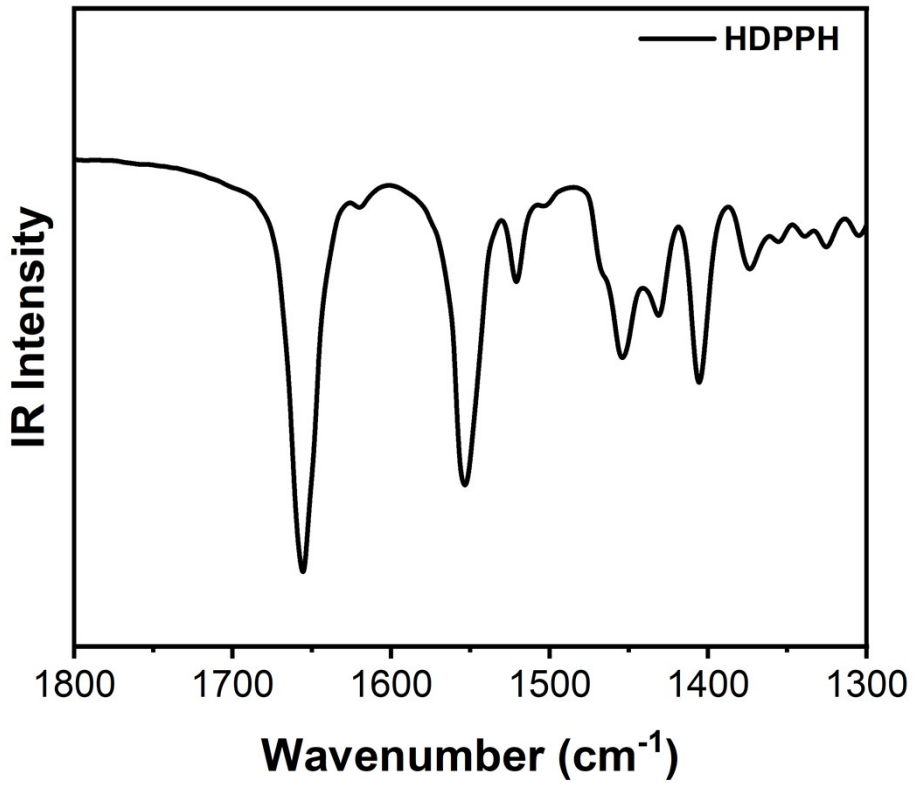

Figure S19. ATR-IR spectrum for **HDPPH** as solid powder.

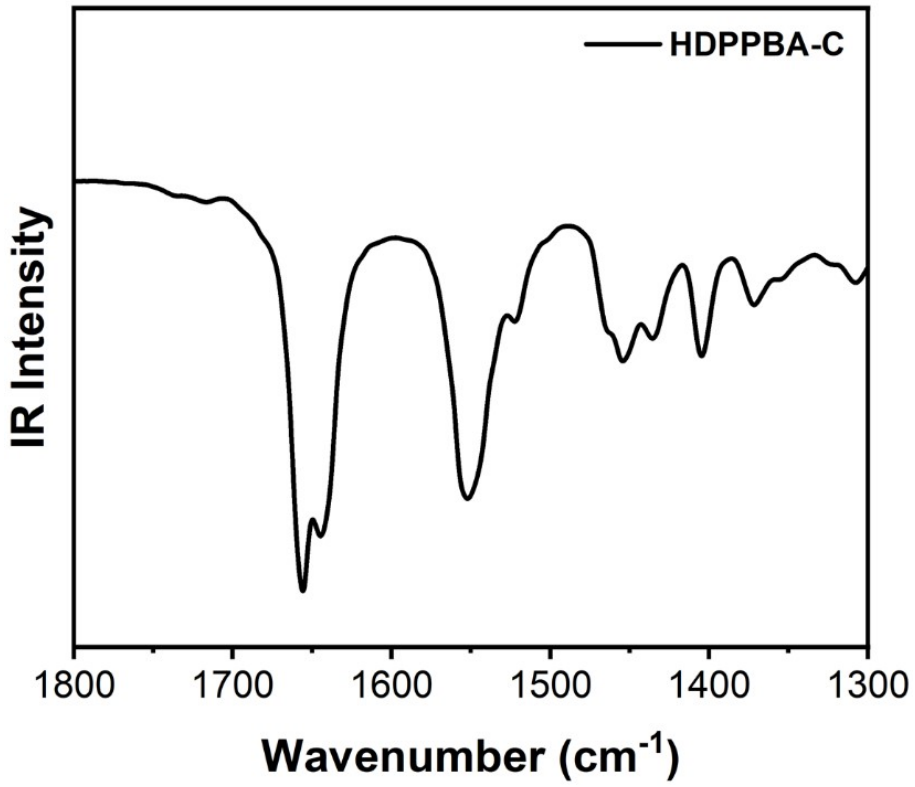

Figure S20. ATR-IR spectrum for **HDPPBA-C** as solid powder.

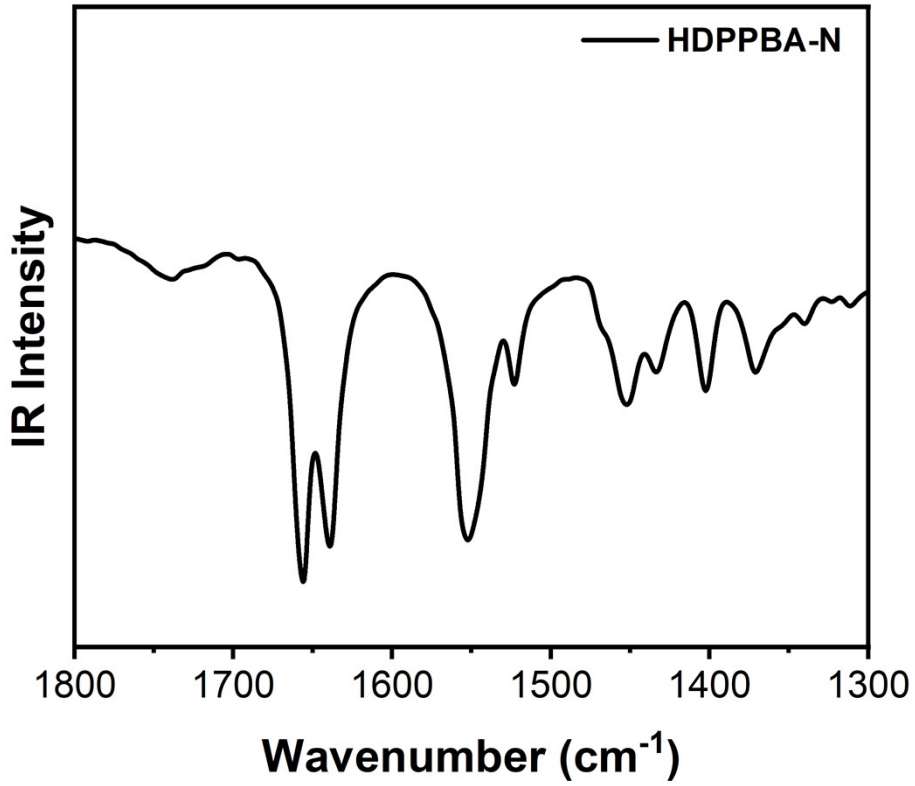

Figure S21. ATR-IR spectrum for **HDPPBA-N** as solid powder.

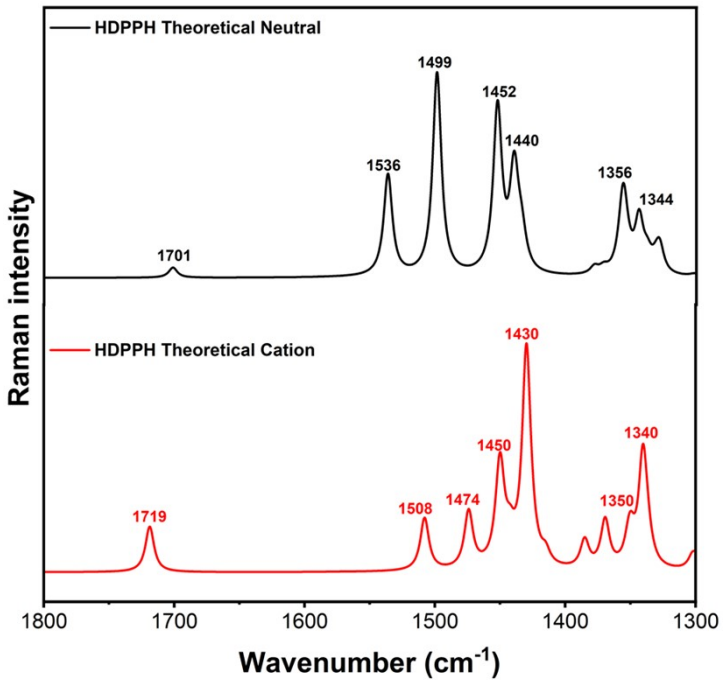

Figure S22. B3LYP/6-31G** Raman theoretical spectra (*f*=0.96) for **HDPPH.** Black for neutral state and red for radical cation state.

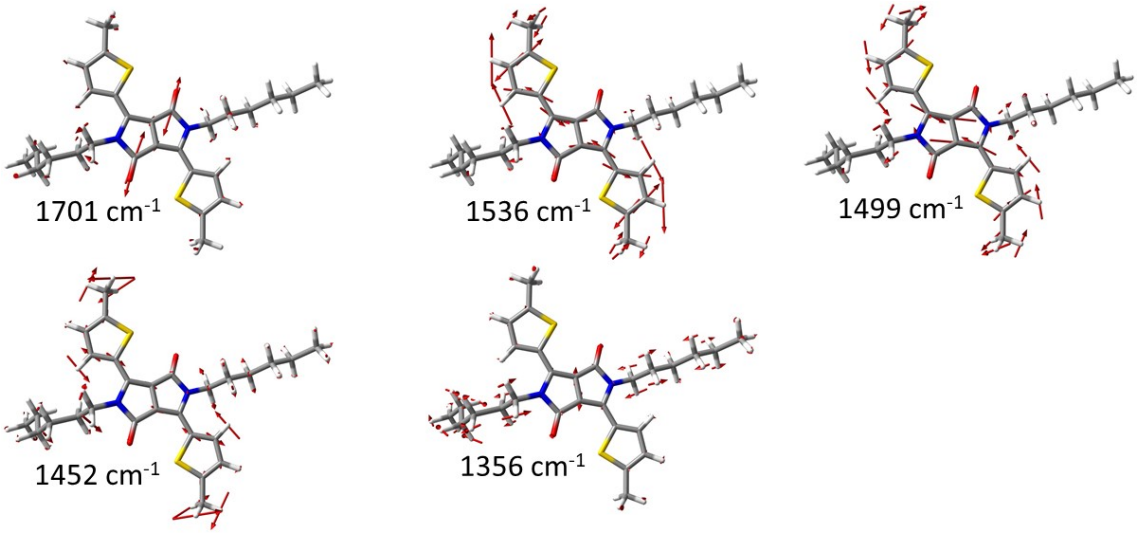

Figure S23. B3LYP/6-31G** Raman predicted eigenvectors for **HDPPH** in neutral state.

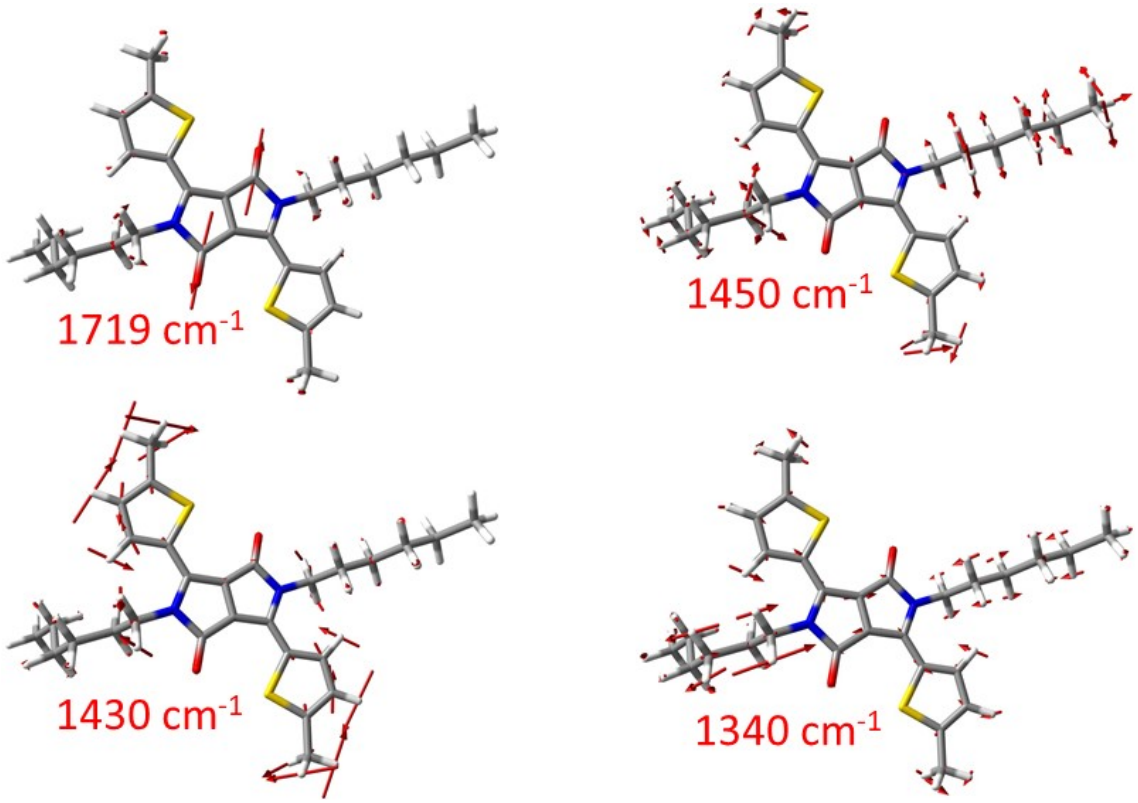

Figure S24. B3LYP/6-31G** Raman predicted eigenvectors for **HDPPH** in radical cation state.

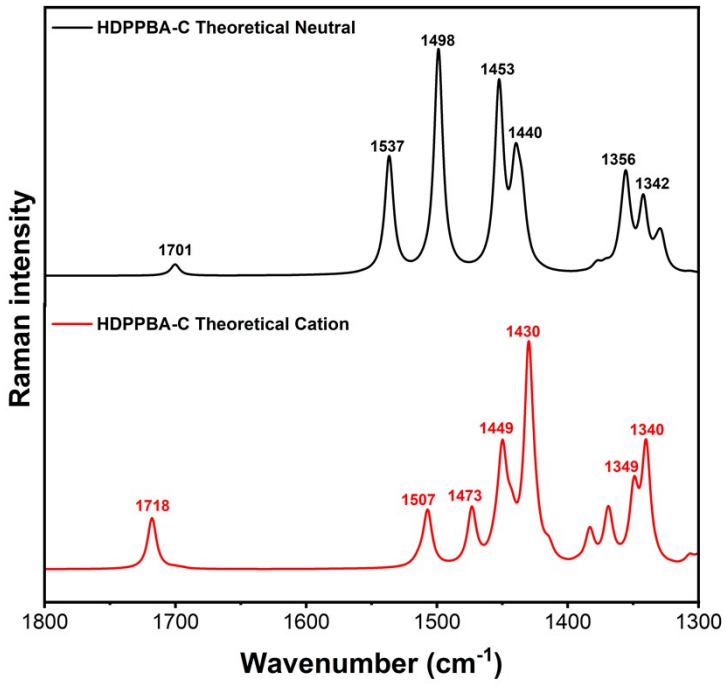

Figure S25. B3LYP/6-31G** Raman theoretical spectra (*f*=0.96) for **HDPPBA-C.** Black for the neutral state and red for radical cation state.

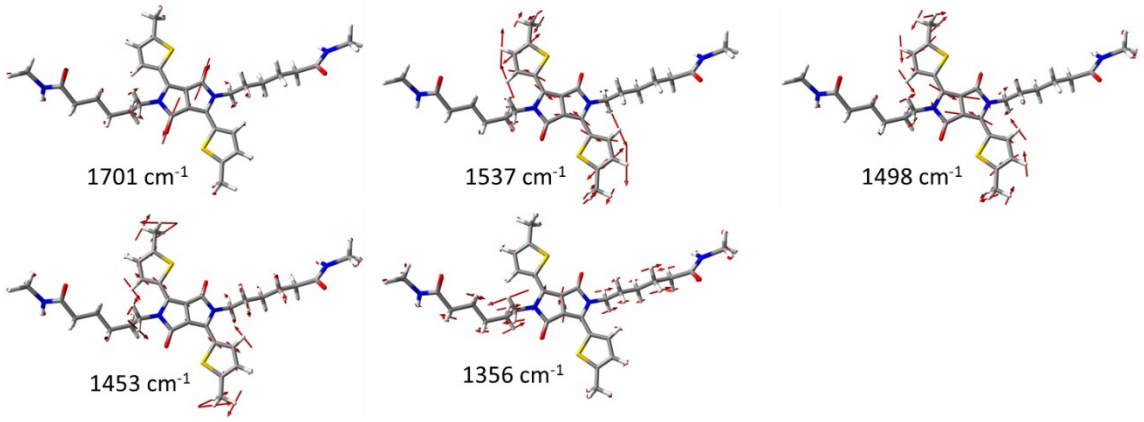

Figure S26. B3LYP/6-31G** Raman predicted eigenvectors for **HDPPBA-C** in neutral state.

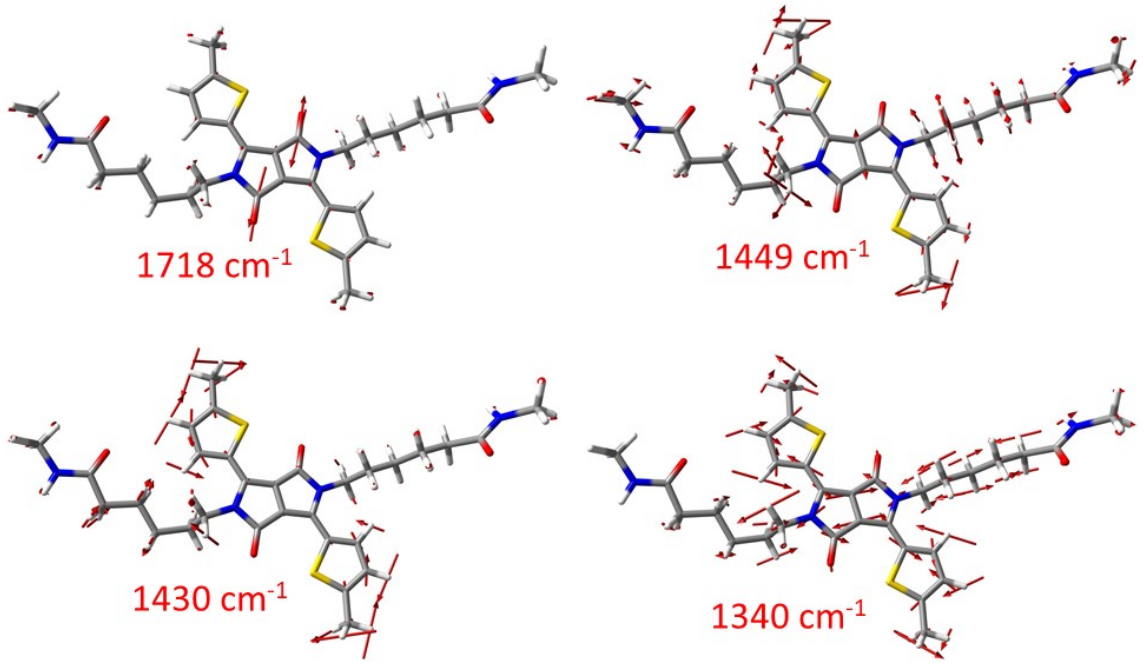

Figure S27. B3LYP/6-31G** Raman predicted eigenvectors for **HDPPBA-C** in radical cation state.

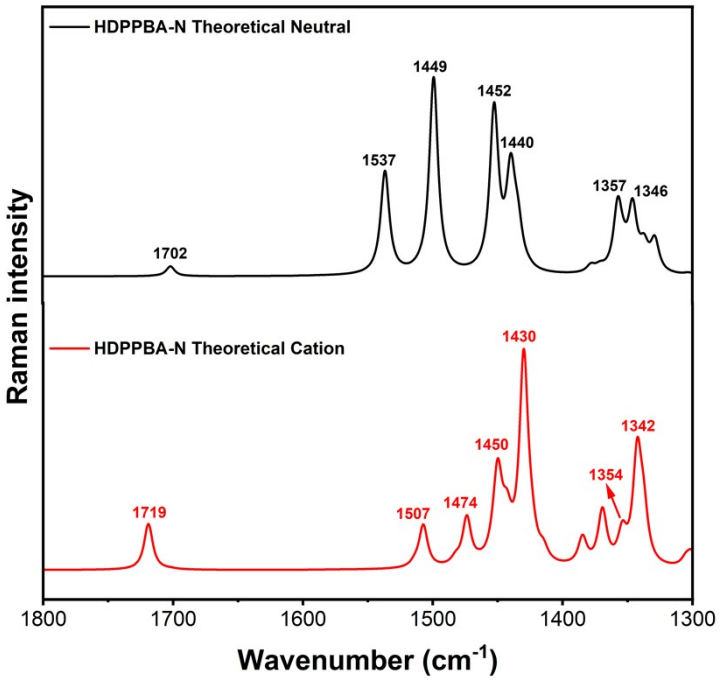

Figure S28. B3LYP/6-31G** Raman theoretical spectra (*f*=0.96) for **HDPPBA-N.** Black for neutral state and red for radical cation state.

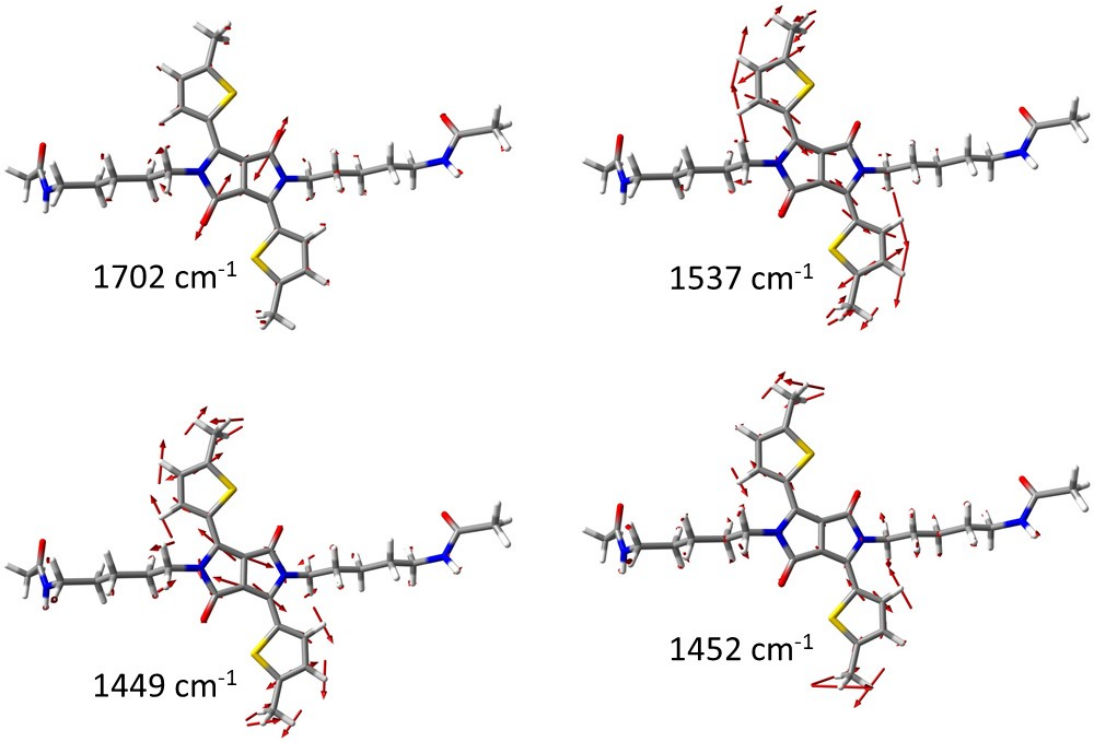

Figure S29. B3LYP/6-31G** Raman predicted eigenvectors for **HDPPBA-N** in neutral state.

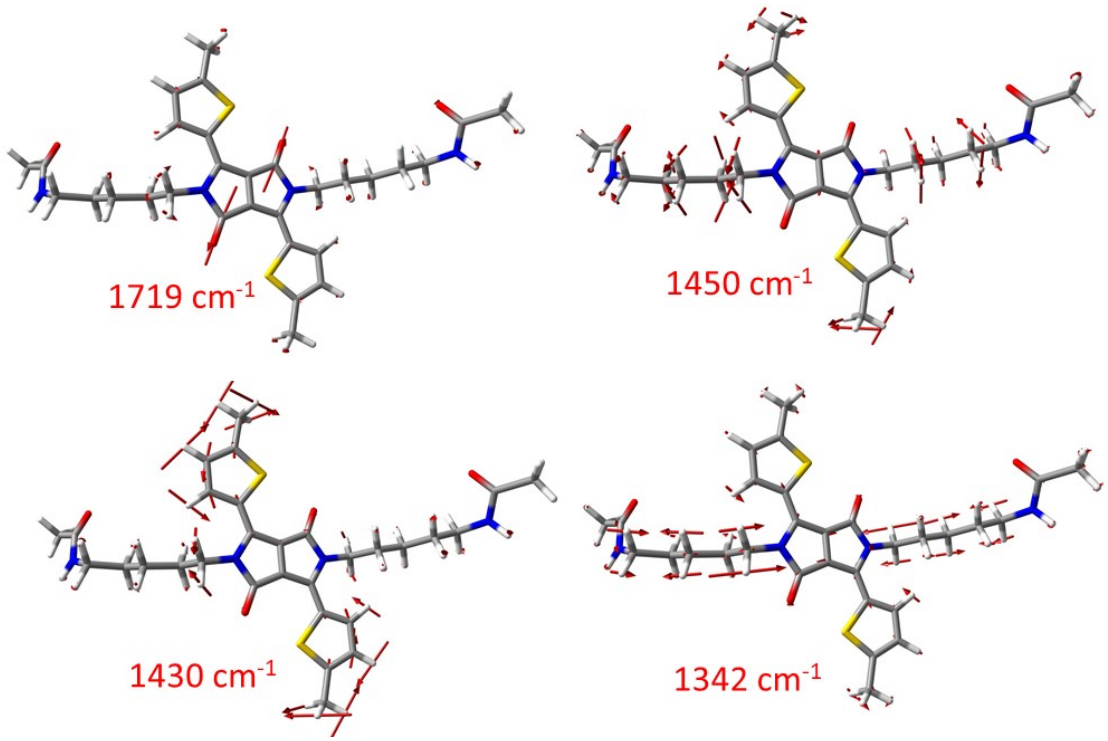

Figure S30. B3LYP/6-31G** Raman predicted eigenvectors for **HDPPBA-N** in radical cation state.

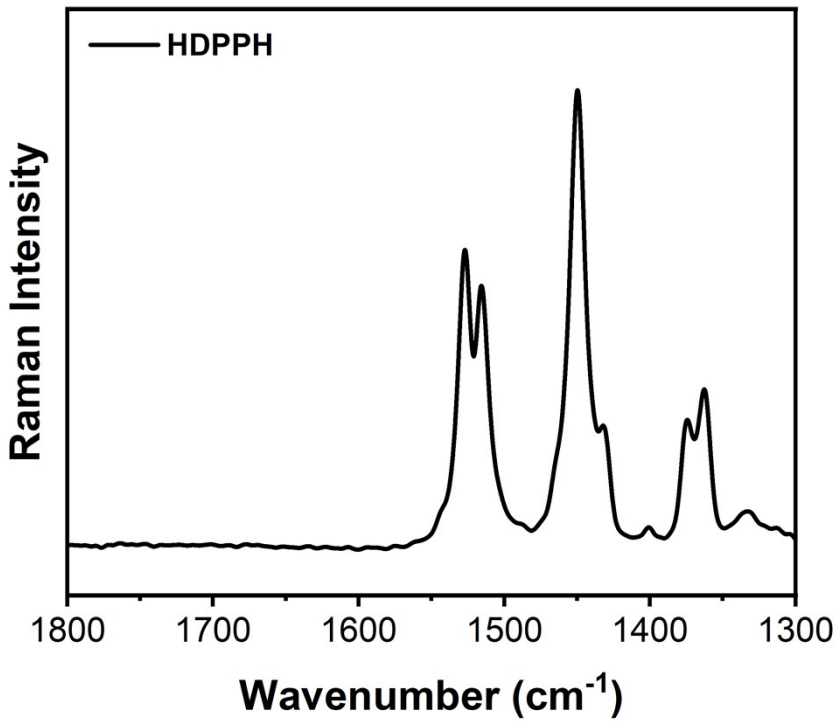

Figure S31. FT-Raman spectra for **HDPPH** as bulk powder

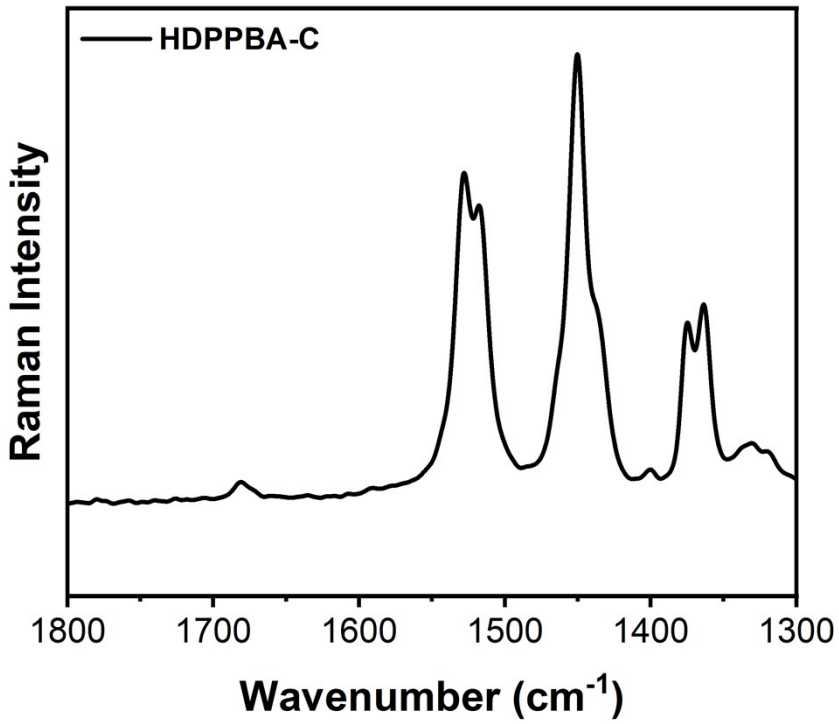

Figure S32. FT-Raman spectra for **HDPPBA-C** as bulk powder

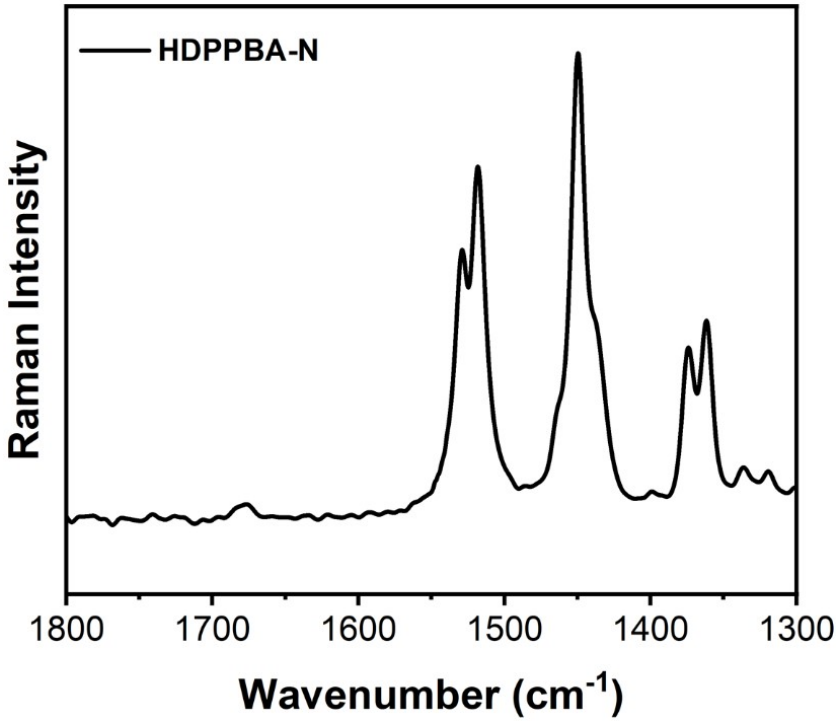

Figure S33. FT-Raman spectra for **HDPPBA-N** as bulk powder

6. Spectroelectrochemistry

In order to analyze the appearance of charged species, Figures S29-S31 show the evolution of the spectra in UV-Vis/NIR, for the compounds **HDPPBA-C**, **HDPPBA-N** and **HDPPH**, obtained after progressive electrochemical oxidation at low concentration ($7x10^{-4}$M) in presence of an electrolyte as support ((n-Bu)4NPF6). The diluited solution was introduced in an Optically Transparent Thin-Layer Electrochemical (OTTLE) cell positionetd in the sample compartment of a Cary 500 spectrophotometer. This spectroelectrochemical cell is based on a transparent thin-layer of quartz and three electrodes: a Pt gauze as the working electrode, a Pt wire as the counter electrode and an Ag wire as the pseudo-reference electrode. Both, the amide compounds (**HDPPBA-C** and **HDPPBA-N**) as the control compound (**HDPPH**) show the same UV-Vis spectral profile, where the neutral spectrum (black curve) shows a absorption bands at 356, 520 and 560 nm. As the potential increases, the spectral profile of the neutral compound evolves to the formation of a new profile where the appearance of two new bands around 640 nm and 879 nm. These new peaks are associated with the formation of cationic species, which is predicted quite well by theoretical calculations at the TD-DFT level. No remarkable changes are appreciated for the three molecules under, since we are working with dilute solutions where intermolecular interaction are minimal.

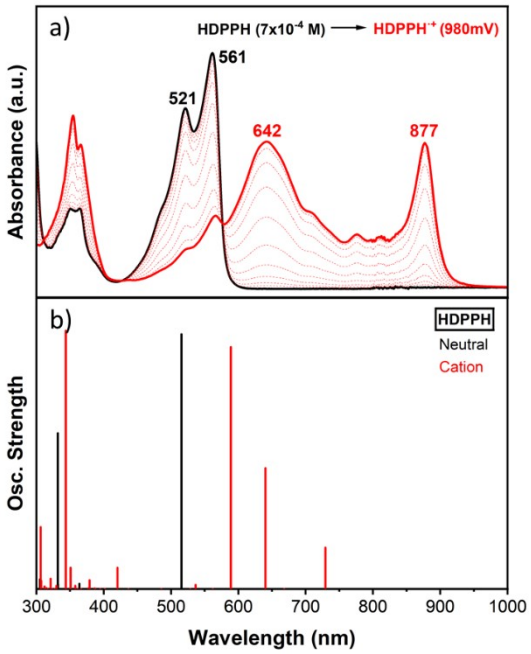

Figure S34. a) UV-Vis-NIR absorption spectra of **HDPPH** electrochemically oxidized by progressive increase of the oxidation potentials; b) TDDFT-B3LYP/6-31G**-calculated vertical transition energies.

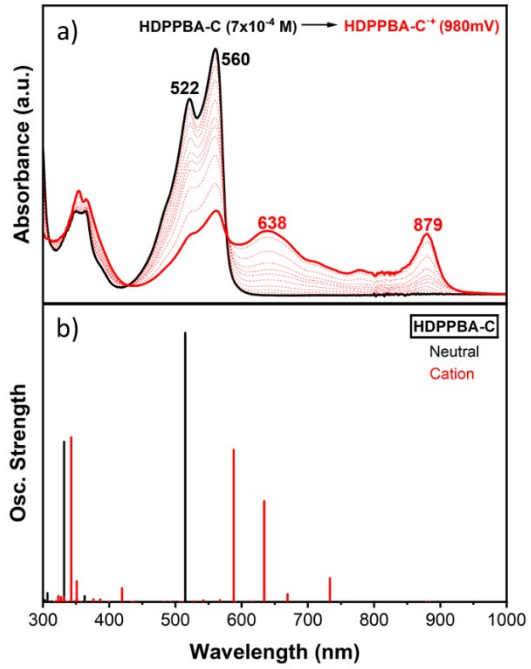

Figure S35. a) UV-Vis-NIR absorption spectra of **HDPPBA-C** electrochemically oxidized by progressive increase of the oxidation potentials; b) TDDFT-B3LYP/6-31G**-calculated vertical transition energies.

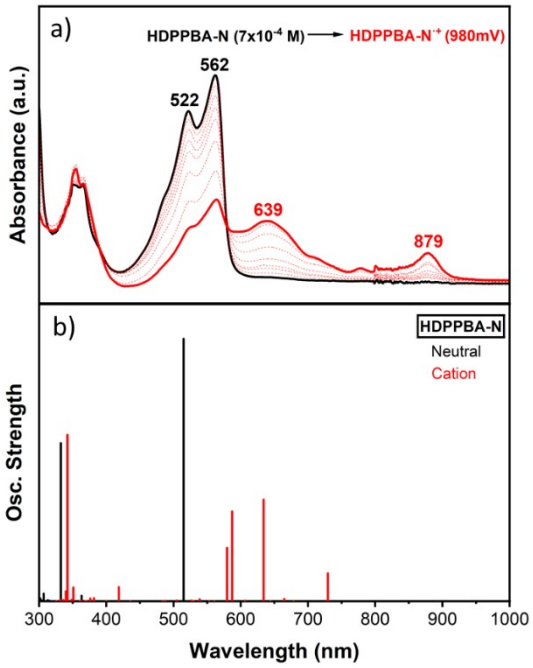

Figure S36. a) UV-Vis-NIR absorption spectra of **HDPPBA-N** electrochemically oxidized by progressive increase of the oxidation potentials; b) TDDFT-B3LYP/6-31G**-calculated vertical transition energies.

7. References

[1]. Avila-Rovelo NR, Martinez G, Matusda W, Sinn S, Leveque P, Schwaller D, Mésini P, Seki S, Ruiz-Carretero A. J. Phys. Chem. C 2022, 126, 10932-10939. doi: 10.1021/acs.jpcc.2c03105

[2]. Lee C, Yang W, Parr RG. Development of the Colle-Salvetti correlation-energy formula into a functional of the electron density. *Phys Rev B*. 1988;37(2):785. doi:10.1103/PhysRevB.37.785

[3]. Becke AD. Density-functional thermochemistry. III. The role of exact exchange. *J Chem Phys*. 1998;98(7):5648. doi:10.1063/1.464913

[4]. Hehre WJ, Ditchfield K, Pople JA. Self—Consistent Molecular Orbital Methods. XII. Further Extensions of Gaussian—Type Basis Sets for Use in Molecular Orbital Studies of Organic Molecules. *J Chem Phys*. 2003;56(5):2257. doi:10.1063/1.1677527

[5]. Francl MM, Pietro WJ, Hehre WJ, et al. Self-consistent molecular orbital methods. XXIII. A polarization-type basis set for second-row elements. *J Chem Phys*. 1998;77(7):3654. doi:10.1063/1.444267